On the representation of shallow convection in the trades by large-domain, hecto-meter, large-eddy simulations

Hauke Schulz[1,2], Bjorn Stevens[1]

[1]Max Planck Institute for Meteorology, Hamburg, Germany
[2]University of Washington/CICOES, Seattle, WA, USA

Key Points:

- A 41 day, hm-scale simulation is run to quantify meso-scale variability in cloudiness in the downstream trades.
- The simulated cloudiness co-varies with precipitable water, temperature and wind speed mimicking the observations.
- The vertical distribution of cloudiness remains challenging at the cost of representing mesoscale patterns with stratiform cloud amount.

Corresponding author: Hauke Schulz, `haschulz@uw.edu`

Abstract

The meso-scale variability in cloudiness of the marine trade-wind layer is explored with large-eddy simulations of regional extent and validated against observations of the EUREC^{4}A field campaign. 41 days of realistically forced simulations present a representative, statistical view on shallow convection in the winter North Atlantic trades that includes a wide range of meso-scale variability including the four recently identified patterns of spatial organization: *Sugar*, *Gravel*, *Fish* and *Flowers*. The results show that cloud cover is on average captured well but with discrepancies in its vertical and spatial distribution. Cloudiness at the lifting condensation level depends on the model resolution with the finer one producing on average a more realistic cloud profile. Independent of the resolution, the variability in cloudiness below the trade inversion is not captured, leading to a lack of stratiform cloudiness with implications on the detectability of meso-scale patterns whose cloud patches are characterized by stratiform clouds. The simulations tend to precipitate more frequently than observed, with a narrower distribution of echo intensities. The observed co-variability between cloudiness and environmental conditions is well captured.

Plain Language Summary

Clouds generally cool the planet due to their ability to reflect sunlight efficiently. To estimate this cooling in a future climate, the processes leading to cloud formation need to be understood. A process that current climate simulations struggle to capture due to their coarse resolution is the variability and patterning of cloudiness on scales on the order of 10-100km. In this study we ran higher resolved simulations at hm-resolutions by limiting the region to the downstream North Atlantic trades where the patterning of shallow clouds is common. Coinciding our simulations with the measurements of the EUREC4A field campaign and being able to run them for over a month allowed us to pinpoint current deficits that these higher resolved simulations have. These are in particular the vertical cloud distribution with too little stratiform cloud amount and too much precipitation that hardly changes with the patterning in cloudiness. Nevertheless, the simulations do a good job in capturing the day-to-day variability in total cloud cover and its co-variability with environmental conditions justifying a further study of the phenomenon with these kind of simulations and ultimately improving the climate simulations on this aspect.

1 Introduction

Clouds associated with shallow maritime convection have been recognized as a vital contributor to the net cloud radiative effect for decades (Bony & Dufresne, 2005, Hartmann et al., 1992). Both small areas with large cloud fractions and large areas with small cloud fractions, make important contributions to these effects. The eastern ocean basins, where cold ocean currents and the overlying warm air give rise to extensive cloud decks, is an example of a small area with a large coverage of clouds. The trade-wind regions typify the idea of a large region with a relatively small coverage of clouds. Often these limiting cases are idealized as end points of a continuous transition, as overcast regions break-up into scattered, randomly distributed, cumulus convection as air-masses are advected over warmer waters by the trade winds.

Nature is more messy, as even in the downwind trades cloudiness can vary considerably, something that Riehl (1954) already pointed out. And although scattered, seemingly random, distributions of rather shallow clouds, are observed in the downstream trades, the prevalence of such cloud regimes might have been over-emphasized by modeling studies on domains too small to capture meso-scale forms of organization (Siebesma et al., 2003, vanZanten et al., 2011). As more modern observations began documenting variability in the forms of organization of clouds in the trades (Rauber, Ochs, et al., 2007), and it became possible to simulate clouds using fine-meshes on larger (but still not particularly large) domains (Heus & Seifert, 2013), attention began to focus on what determines how shallow convection organizes, and how this influences cloud amount (Bretherton & Blossey, 2017).

More recently research has demonstrated that variations in cloudiness in the downstream trades can often be associated with recognizable meso-scale patterns (Stevens, Bony, et al., 2020), and how these patterns help explain differences in cloud-radiative effects (Bony et al., 2020). Using observations, Schulz et al. (2021) has further demonstrated that these patterns encompass different cloud morphologies which emerge in association with distinct meteorological environments. These findings support the idea that changes in cloud amount with warming might be realized by a different selection of large-scale conditions, and hence a change in the mix of mesoscale cloud patterns, a possibility that is all the more intriguing because state-of-the-art climate models do not account for this variability (Nuijens et al., 2015).

To understand the factors that influence clouds in the trades, Large Eddy Simulation is a useful tool; all the more so as it has now become possible to perform relatively fine mesh simulations over very large (ca. 1000 km) domains for periods of days (Stevens, Acquistapace, et al., 2020). Notwithstanding the attractiveness of the approach, the literature assessing the fidelity of the cloud representation by LES is surprisingly sparse. Arguably there is only one single study that *quantitatively* assesses the ability of LES to represent the structure of the cloud-topped boundary layer, and that is a case-study of a stratocumulus-topped boundary layer as observed during DYCOMS2 (Stevens et al., 2003, 2005). Attempts to similarly assess LES in cloud regimes more characteristic of the downstream trades have not been successful. Even without a consideration of the mesoscale patterning of the clouds, the lack of quantitative information about clouds (Siebesma et al., 2003, Stevens et al., 2001), and/or uncertainty as to the state of the large-scale environment (vanZanten et al., 2011), have hindered efforts to assess the fidelity of the LES.

EUREC^{4}A was devised in large part to address this knowledge gap. One of its two primary objectives was: "To provide a reference data-set that may be used as a benchmark for the modelling and the satellite observation of shallow clouds and circulation" (Bony et al., 2017). To accomplish this objective a very large number of both complementary and redundant cloud observations were assembled during EUREC^{4}A. The campaign also made use of extensive soundings (2614 soundings were dropped or launched in total) in ways that allowed to characterize the meso-scale (200 km) environment (Bony & Stevens, 2019) upwind of the Barbados Cloud Observatory (Stevens et al., 2021). In this paper we use a subset of the EUREC^{4}A measurements to test the ability of numerical simulations over large domains, with fine (156 m to 624 m) grids, to represent the observed cloud fields and their co-variability with their meso- to large-scale environment. More precisely we ask:

1. To what extent do the simulations capture the mean features of the observed cloud field?
2. How well do the simulations reproduce the observed variability in cloudiness, particularly in relation to meso-scale patterns of cloudiness and its co-variability with the meteorological environment.

In addressing these questions we highlight the strengths and weaknesses of state-of-the-art LES, and identify the limitations that future work must overcome to get the most out of the technique. We proceed as follows: Section 2 describes the simulation configurations, observations and the forward operators used to better compare the simulation output with measurements. Section 3 discusses the similarities of cloudiness in Large Eddy Simulation (LES) and observations. We conclude with Section 4.

2 Data and Methods

2.1 Simulations

We focus on the downwind trades of the North Atlantic during January - February 2020, a period when this area has been intensively sampled as part of the EUREC^{4}A field campaign (Stevens et al., 2021). We conducted simulations with the ICOsahedral Nonhydrostatic (ICON) model family (Dipankar et al., 2015, Gassmann, 2013, Wan et al., 2013, Zängl et al., 2015) at gridspacings of 1.25 km (ICON-SRM), 624 m (ICON-624m), 312 m (ICON-312m) and 156 m (ICON-156m). With the exception of the storm-resolving simulation (ICON-SRM), which is used for the initialization and to provide lateral boundary conditions for the finer mesh, all simulations are based on the large-eddy simulation capabilities as in Heinze et al. (2017). This branch of the model is called ICON-LEM in the remainder of the manuscript.

The configuration of the different simulation domains, and how they are forced is summarized with the help of Table 1. The ICON-LEM domains (Fig. 1) are extended in the east-west direction to better align with the trade-winds and thereby maximize the temporal coverage of the evolution of the shallow convection. The eastern boundaries of the nested domains decrease with each refinement by at least two degrees to reduce the possibility of numerical artifacts entering the domain with the prevailing easterly trades. On the western boundaries less of a margin is provided, as inflow from the west only occurs at upper levels, and thus at most affects high-clouds, which were infrequent and showed little sign of influencing low-level cloudiness.

The simulations were designed so that even the smallest (ICON-156m) domain would be large enough to capture meso-scale variability in its full extent, including all four of the mesoscale patterns observed and defined by Stevens, Bony, et al. (2020). As such the ICON-156 domain extends over 9.75° of longitude and 5.00° of latitude, and thereby cov-

Table 1. Overview about used simulation configurations.

Model	ICON-SRM	ICON-624m	ICON-312m	ICON-156m
No. grid cells x levels	6773696 x 75	4528560 x 150	11792076 x 150	24469588 x 150
hor. gridspacing*	1248 m	624 m	312 m	156 m
ver. gridspacing (lowest level/ 1000 m/ 2000 m)	20 / 140 / 190 (150 levels)	20 / 70 / 85 (150 levels)	20 / 70 / 85 (150 levels)	20 / 70 / 85 (150 levels)
Model top (km)	35	21	21	21
hor. domain	67W - 43W, 0N-24N	60.25W - 45W, 7.5N - 17N	60W - 47W, 9N - 16.25N	59.75W - 50W, 10.5N - 15.5N
Forcing (except SST)	ECMWF IFS (hourly)+	hourly ICON-SRM	one-way online nesting	
Forcing (SST)	ECMWF IFS (fixed at initial time)	continuously (linear interp. from 1h ERA5 SKT)		
restart	daily at 00 UTC	none		
Turbulence	turbulent kinetic energy (TKE)	Smagorinsky diffusion		
Microphysics	One moment incl. graupel (Baldauf et al., 2011)	Two moment (Seifert & Beheng, 2006)		
Cloud-scheme	Fractional cloud cover	All-or-nothing		
Radiation	RRTM (Mlawer et al., 1997, Stevens et al., 2013)			

* edge lengths of triangular grid cells

+ analysis at 00;12 UTC ; otherwise IFS forecast

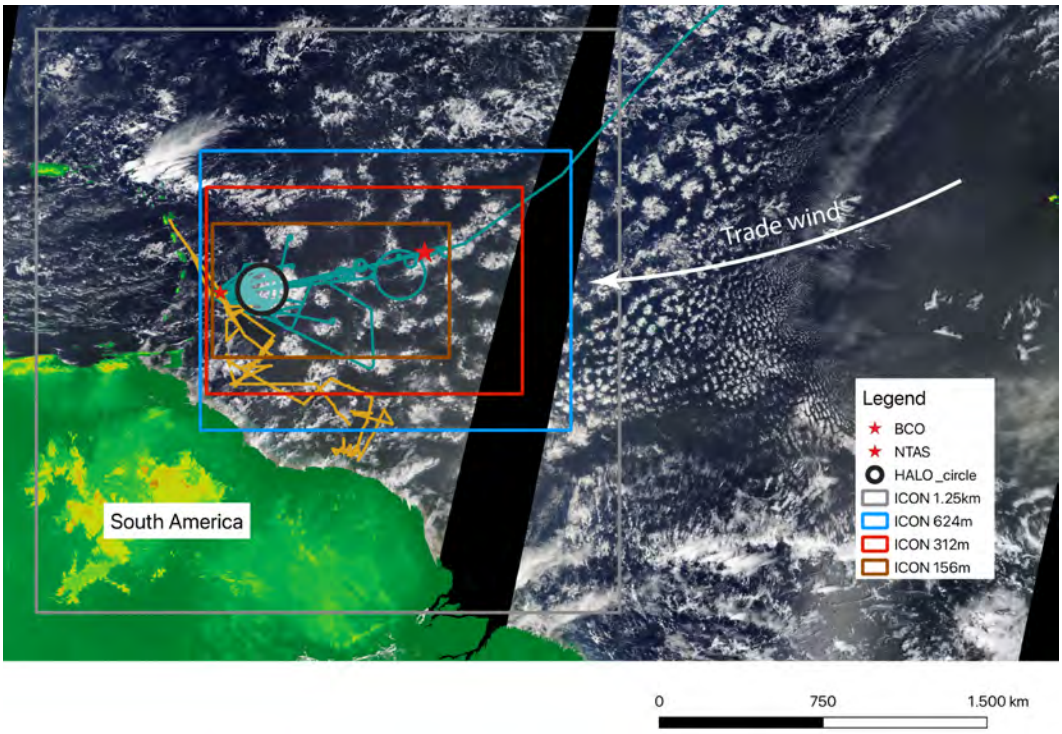

Figure 1. Overview of simulation domains ICON-SRM (gray), ICON-624m (blue), ICON-312m (red), ICON-156m (brown). The tracks of the platforms HALO and L'Atalante, which are representative for the two different measurement foci of the EUREC^{4}A campaign are shown in orange and purple, respectively. EUREC^{4}A-circle is shown in black. The location of the BCO and the NTAS buoy are marked with a red star at the western and eastern part of the domain, respectively. For a sense of scale, the MODIS image of February 12 is shown with landmasses colored in green to brown depending on height.

ers an area spanning about 1050 km in the east-west direction, and 550 km from the south to the north. This makes our finest-grid domains slightly larger than the fine-grid domain used by Heinze et al. (2017) and several times larger than the expected (ca. 200 km) size of the meso-scale structures we look to represent – as is also evident, for instance, in Fig. 1. For the analysis itself a common domain from 11° N - 15° N and 59.3° W - 55.3° W is used if not stated otherwise.

The simulations were created as follows. First, the ICON-SRM simulations were performed to provide initial and boundary conditions for the LES. The ICON-SRM simulation were initialized daily from the IFS for the period between 9 January and 19 February and run for 40 h, with hourly boundary conditions taken from the IFS. The last 24 h of each of these 40 h forecasts was then used to provide lateral boundary condition for the continuously running ICON-624m simulation, which then provided lateral boundary conditions for a one-way nested ICON-312m simulation, and so on. For the lower boundary, sea skin temperatures were updated every timestep based on linearly time-interpolated hourly ERA5 skin temperatures. Skin temperatures were chosen over SST because ICON does not have a skin temperature parameterization. There is a possibility that the use of the ERA5 SST biases the simulations. Compared to the SST measured by the R/V Meteor, the ERA5 SST is on average 0.4 K colder. The use of the skin-temperature introduces another 0.2 K suppression. If the cool skin-temperature estimated by the surface flux schemes used by the ERA5 over-states this effect (and there are some indications that it does) this could result in the SSTs being as much as 0.6 K colder than observed. A comparison of SSTs measured by the R/V Ronald H. Brown, and Saildrones, which operated on an area beyond the EUREC^{4}A-circle, showed biases ranging from −0.4 K-0.2 K (Wick et al., 2023), putting our estimates of biases near the cold end of what they record. Attempting to correct these biases is however difficult, as doing so introduces the possibility of introducing inconsistencies with the lateral boundary conditions and pressure gradients of the re-analysis. For this reason we simply note the discrepancy and return to its possible effects in the context of analyses where it might have some bearing on the results.

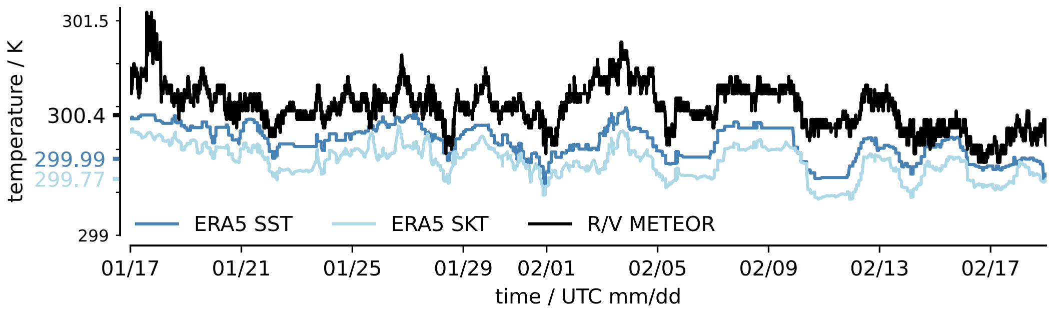

Figure 2. Comparison of the simulation's surface boundary conditions based on ERA5 skin-temperatures (SKT) to ERA5 foundation temperatures (SST) and measurements taken on-board the R/V Meteor at a depth of 2.1 m. For better comparison the nearest grid-cells of the model to the ship's track along its north-south transects at 57.245°W are used. Note that the sub-daily variations of ERA5 SSTs are caused by this sampling strategy and are constant in space and time within a day.

The above procedure required the ICON-LEM simulations to be initialized only once. The ICON-624m was initialized from the ICON-SRM at 10 UTC on January 9th, and then used to initialize the ICON-312m 6 h later. Output after midnight of January 10, 2020 is used in the analysis.

The method chosen for specifying the lateral boundary conditions for the ICON-624m simulations introduces a discontinuity at 16 UTC during the transition from one day's ICON-SRM forecast to the next days. This discontinuity is expected to be small – indeed we see no apparent impact of this daily 're-alignment' of the boundary conditions in our analysis – as the ICON-SRM is continually updated by the reanalysis at its lateral boundaries. Re-initializing the ICON-SRM each day, however, helps ensure that the large-scale conditions, and hence the lateral boundary conditions provided to the ICON-624m simulation, remain well aligned with what was observed.

An additional nest at 156m grid-spacing, ICON-156m, is included for the period of February 1 to February 7. The roughly ten-fold greater computational intensity of this configuration precluded a longer simulation.

2.1.1 Satellite forward simulator

To better compare the output of the LES with satellite observations, we rely on the RTTOV forward simulator (Saunders et al., 2018), which is designed to emulate satellite images based on simulation output. In this study, we use the Geostationary Operational Environmental Satellite (GOES)-16 Advanced Baseline Imager (ABI) specifications to compare them to the actual satellite's instrument, which covers the region of interest with a high temporal and spatial sampling of 10 min and 2 km (channel 13: 10.35 µm), respectively. In an attempt to get the most consistent synthetic satellite images, we made modifications to the most recent version of ICON (2.6.3). These modifications include design changes that let us use RTTOV v13 during the run time of ICON and reduce the amount of data that needs to be saved to disk for offline calculations. In addition, we use the calculated two-moment microphysics to feed both the internal RRTM radiation scheme and the one of RTTOV to make their input consistent.

The synthetic satellite images are calculated every 10 minutes to match the temporal resolution of the ABI instrument. A snapshot of the animation (`https://doi.org/`

10.5281/zenodo.7567204) that visualizes the actual and synthetic satellite images for the complete time period is shown in Fig. 3.

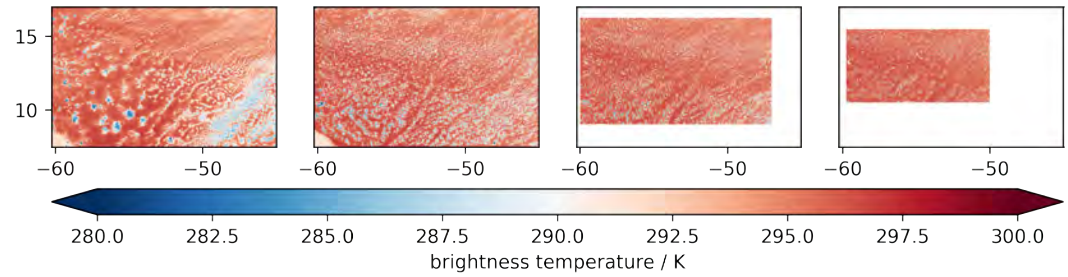

Figure 3. Snapshot of GOES-16 ABI channel 13 satellite image (left) and the synthetic counterparts from ICON-624m, ICON-312m and ICON-156m (from left to right) for February 2, 2020 at 7:50 UTC. Full animation available at `https://www.doi.org/10.5281/zenodo.7567204`.

2.1.2 Radar forward simulator

Past work has emphasized how the trade-wind boundary layer is sensitive to the distribution of cloudiness in the vertical (Brient et al., 2016, Nuijens et al., 2014, Vogel et al., 2022). Likewise, different patterns of mesoscale variability have been shown to be associated with different vertical profiles of cloudiness (Schulz et al., 2021), but past work suggests that it proves difficult for simulations to robustly capture this structure (Atlas et al., 2020, Stevens et al., 2001) even when not conditioned on different patterns of cloudiness.

Hence in evaluating the fidelity of the LES we also compare the vertical profiles of the simulations to observations. For this purpose we use a forward simulator to resemble the vertical distribution of cloudiness as seen by the Ka-Band radar positioned at the Barbados Cloud Observatory (BCO) (see next section), as this is well situated at the downstream end of our domain, and was also used in the study by Schulz et al. (2021).

We rely on the radiative transfer simulator PAMTRA (Passive and Active Microwave TRANsfer package) (Mech et al., 2020) as it has successfully been used with the same radar frequency in earlier studies in this region (Jacob et al., 2020). PAMTRA has been configured similar to Mech et al. (2020) to match the two-moment microphysics scheme of Seifert & Beheng (2006) which has been used in the LES of this study. Hence, PAMTRA is able to infer the original particle size distribution assumed by the simulations from its bulk measures of mixing ratio and number concentration, which are saved every 60 s at the location of the BCO. PAMTRA therefore simulates reflectivities that are nominally consistent with the microphysical state of the LES. Although the higher moments of the hydrometeor distribution are not strongly constrained by the bulk schemes used to model cloud microphysics, our use of the PAMTRA based reflectivities is limited to the creation of a rain and cloud mask, which should limit the impact of ambiguities in the forward model.

2.2 Observations

2.2.1 EUREC^{4}A Observations

Among the tremendous amount of observation platforms that were present in the simulated area during the EUREC^{4}A time period, the Barbados Cloud Observatory (BCO), was a fixed point. The BCO is situated at Deebles Point, a windward promontory on Barbados (Stevens et al., 2016), an island situated near the western boundary of our simulation domains. We used the measurements from the BCO's vertically pointing Ka-band radar CORAL to detect the vertical distribution of hydrometeors. Averaging these measurements in time results in echo fractions which are a combined measure of cloud fraction and precipitation fraction. A threshold of -50 dBZ has been applied to exclude backscatter from deliquesced large sea-salt aerosols near the lifting-condensation level (Klingebiel et al., 2019).

Measurements from radiosondes launched from the BCO and ships, as well as extensive (1068) dropsondes launched from aircraft along the EUREC^{4}A-circle (up-wind of the BCO, as shown in Fig. 1)(George et al., 2021) were integrated into the global observation system to help constrain the large-scale analysis from which boundary conditions for the ICON-SRM are derived. In the past, there had been the concern that the large-scale vertical winds from the reanalysis winds would not be representative of the observed conditions. George et al. (2022) demonstrates that the mean large-scale vertical motion observed across the EUREC^{4}A-circle agrees well with the analysis, also when the sondes were not included, giving confidence in the ability of the analysis to capture the large-scale conditions.

Other measurements, for instance from the vertical profiling radars on the R/V Meteor and on the R/V Ronald H. Brown, from passive microwave radiometers and Raman lidars that were situated at the BCO and on the R/V Meteor, remote sensing by the low-flying ATR and the high-flying HALO as well as in-situ measurements from the Twin Otter and the ATR-42 would provide additional points of reference for the simulated cloud amounts. These measurements are, however, not necessary to answer the questions we pose in this study, and are more difficult to compare to the simulations due to the mobility of the platforms, and the difficulty of generating high-frequency output that tracks the location of the platforms. Nonetheless, based on an identification of the simulation challenges, this output will be useful for more detailed analyses of further, more targeted simulations, also to investigate how well the downstream evolution of the boundary layer and the boundary layer cloud structure (for instance when the R/V Ronald H. Brown, the R/V Meteor and the BCO were aligned along trade wind trajectories) is captured by the LES.

2.3 Classifications of meso-scale patterns

This study uses two approaches to identify the meso-scale patterns of shallow convection. First, for identifying the days with observed canonical meso-scale patterns, we rely on the manual classifications done by the scientific community of the EUREC^{4}A field campaign as described in Schulz (2022). The scientists inspected satellite images captured during the EUREC^{4}A time period and labeled regions containing *Sugar*, *Gravel*, *Flowers* or *Fish*. The result of this classification for the analysis region, by day, is shown in Fig. 4. These days are used to sub-sample the simulations so as to test their ability to match the characteristics of the observations in conjunction with the observation of specific patterns.

Second, we classified the simulations themselves to test whether the patterns might occur similar often but at different times and locations due to slightly different environments, or simply as a result of internal variability that is poorly constrained by the larger-scale conditions. For this purpose, we classified both simulations and observations using the neural network that has been successfully used in Schulz et al. (2021). The neural network has been trained to detect the cloud patterns in GOES-16 ABI infrared images. To apply the neural network to the simulations we used the output of the RTTOV forward simulator as discussed above.

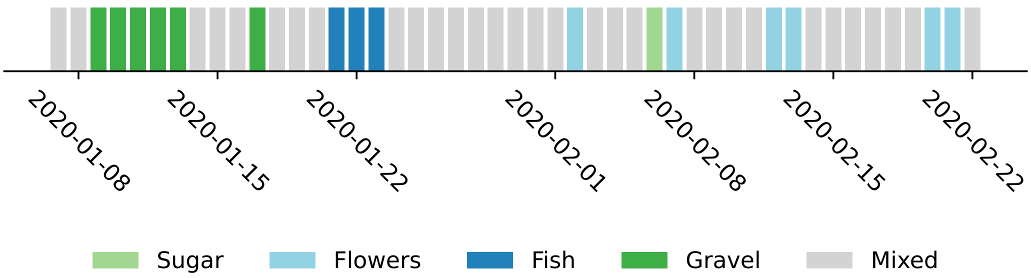

Figure 4. Prevailing meso-scale patterns identified by the EUREC^{4}A community in GOES-16 ABI infrared satellite images (Schulz, 2022), here shown for the analysis region.

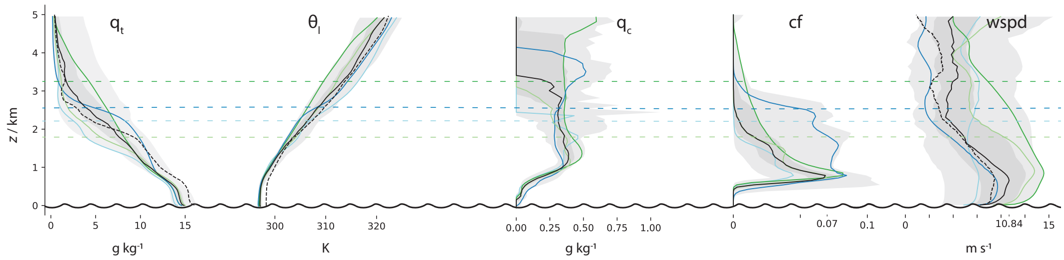

Figure 5. Variability of the simulated trade-wind boundary layer illustrated by median (black profile) and minimum/maximum (light grey) and 25/75th percentile (dark grey) of daily median profiles for total water specific humidity (q_t), liquid water potential temperature (θ_l), cloud water specific mass (q_c, averaged over cloudy points only), cloud fraction (cf, def. as $q_c > 0.$) and wind speed. Profiles of days with clear meso-scale organization are indicated by colors following the scheme of Fig. 4: *Fish* (January 22), *Flowers* (February 2), *Gravel* (January 12), *Sugar* (February 6). The levels of maximum θ_l gradient (inversion height) are indicated with a dashed line. For a better comparison with the median profile of the campaign's dropsondes (dashed) that were dropped along the EUREC^{4}A-circle from the *HALO (High Altitude and Long Range Research Aircraft)*(George et al., 2021), only the encircled area has been analysed for this figure.

3 Similarity of LES and observations

3.1 Characterisation of environment

Variability in the atmospheric environment, which can reflect the air-mass origins as well as the dynamics of its evolution along the trade-wind trajectory is thought to influence the development of different meso-scale patterns of cloudiness. For instance, Schulz et al. (2021) demonstrated that anomalously warm air-masses, tend to originate from lower latitudes, and result in shallower cumulus clouds (with a vertical extents a couple of 100 meters) which are more likely to be classified as *Sugar*. Air-masses originating at higher latitudes tend to be cooler, and depending on factors such as the strength of the subsidence or the near-surface wind-speed, align with other meso-scale patterns of cloudiness. Thus, in what follows we not only explore to what extent the LES represents the observed structure of the lower troposphere, but also how it varies in association with different meso-scale patterns of cloudiness.

Fig. 5 illustrates the atmospheric boundary layer, its variability within the simulated period, and how it co-varies with meso-scale patterns of cloudiness as identified by the satellite imagery. As such it presents a representative picture of the winter-time trade-wind boundary layer as captured by the large-eddy simulation during the period of EUREC^{4}A. The simulated profiles of specific humidity, potential temperature, and wind-speed are broadly similar to the vertical structure as sampled by the aircraft across the EUREC^{4}A-circle. The observations and simulations document a moist layer of 1.5 km to 3.5 km with elevated wind speeds, and a well mixed sub-cloud layer below about 600 m. On average the simulations show a 1 K cooler and 1 g kg^{-1} drier moist layer, with slightly stronger wind speeds through the bulk of the cloud layer. The reduction in specific humidity in the simulations is consistent with what would be expected were the relative humidity unchanged.[1]. In addition to being absolutely drier, and cooler, the simulations show a more continuous transition between the top of the sub-cloud layer at 600 m and the free troposphere (near 3000 m). The soundings document a stronger hydro-lapse, at about 2 km, and a better mixed cloud layer between 600 m to 1500 m.

Systematic biases can be better quantified by comparing the meteogram output from the LEM with near surface observations from the Meteor. Fig, 6 provides such a comparison for the near surface temperature, humidity and wind-speed. By comparing to the R/V Meteor measurements, we avoid possible distortion associated with the effect of the promontory on which the BCO measurements are situated, and temporal sampling biases, but must contend with the fact that the R/V Meteor moved north and south along a constant line of longitude within the eastern part of the EUREC^{4}A-circle, while the meteogram output was situated a bit to the east, at a fixed position, near the east-

[1] The difference in the specific humidity for a 1 K temperature increase of air at 300 K with a fixed relative humidity of 75 % and a pressure of 1015 hPa is 1 g kg^{-1}.

ern edge of the circle. The comparison confirms the ca. 1 K temperature bias, with a somewhat less pronounced tail toward colder temperatures potentially indicative of less cold-pool activity. The simulated near surface relative humidity is slightly higher than observed, but this might result from a poor resolution of the surface layer. Wind-speeds near the surface are also slightly reduced as compared to the observations, in contrast to what is observed in the bulk of the boundary layer.

When profiles from the simulations are sampled similarly to the observations, the thermodynamic structure above 2000 m agrees better, but as the main biases appear for heights below 2000 m, they cannot be explained by poor sampling. Comparisons of individual flight days, over the 1 Feb. to 7 Feb. period which was also simulated with the 156m nested ICON, showed that (1 K to 1.2 K cold-biases were apparent in the sub-cloud layer on all three flight days (2, 5 and 7 Feb) but $1.0\,\mathrm{g\,kg^{-1}}$ to $1.5\,\mathrm{g\,kg^{-1}}$ dry and $-0.5\,\mathrm{m\,s^{-1}}$ to $0.5\,\mathrm{m\,s^{-1}}$ wind biases were only evident for the first two of these days. In both cases (2 and 5 Feb) the simulated cloud layer was shallower than observed. There is a notable and systematic reduction in the wind-speed bias as the grid-spacing was refined from 623 m to 156 m, but no systematic improvement in the thermodynamic structure.

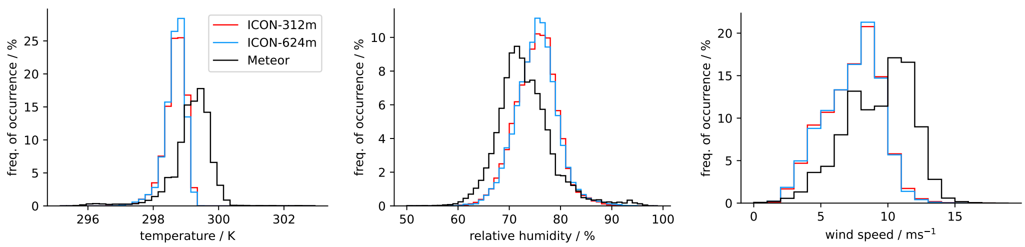

Figure 6. Histograms of temperature (left), relative humidity (middle) and wind speed (right). The observations are based on measurements from the R/V Meteor during its north-south transects at about 57.245°W from 12.1° to 14.5°N. The simulation's quantities are based on the meteogram output at 13.3°N, 56.717°W (eastern circle edge).

The persistence of the cold bias could, in part, be explained by the sea-surface temperatures being prescribed as too cold. Compared to the R/V Meteor measurements, it is hard to make the case for more than a 0.6 K cold bias in the surface temperatures (Fig. 2), which is a factor of two smaller than the bias in near surface air-temperatures, hence other factors seem to be involved. That they are evident for the 2-5 Feb. period helps isolate this time-period for more intensive analysis, perhaps also in comparison with the mixed layer budgets derived from the sounding data by Albright et al. (2022).

Analysis of the different days shows that large changes in the structure of the cloud layer are apparent, as in the observations. The maximum gradient in liquid potential temperature can vary between 1.5 km to 3.5 km and even within a day. These differences are also evident in the variability of the inversion heights, Fig. 5. To some extent the variability is consistent with environmental variations previously noted in association with the differing cloud patterns, with shallower moist layer for *Flowers* and *Sugar*, stronger near surface winds for *Gravel* and increased lower-tropospheric stability in the case of *Flowers*. The *Fish* pattern (January 22) is largely influenced by the cloudy part and to a smaller extent by the clear-sky region. As shown in Schulz et al. (2021) these regions can be in very different atmospheric states, making the comparison less conclusive.

3.2 Meso-scale patterns

3.2.1 Visual inspection

To evaluate the ability of the simulations to capture the mesoscale patterning of the atmosphere we first visually inspect the spatial distribution of clouds, as was done to identify the cloud patterns in the original studies (e.g., Rasp et al., 2020, Stevens, Bony, et al., 2020). In the case of the simulated cloud scenes the visualization is based on the output of the satellite forward operator RTTOV. These simulated scenes are compared to satellite scenes observed at the same time and as shown in Fig. 7 in Fig. 8.

This comparison demonstrates that most of the scenes match the general structure of the patterns with the exception of *Flowers*. At least qualitatively the simulations and observations look more like one another when paired by pattern.

The simulated structure of *Fish* and *Gravel* align best with observations of the same patterns, as shown in Fig. 7. *Fish* shows band structures of cloudy and clear-sky patches and *Gravel* consists of much smaller patches that are roughly arranged in hexagons. Some clouds also rise deeper and produce stratiform clouds that are also visible for this day in the observations. The surface temperature field (not shown) also confirms the frequent and wide-spread occurrence of cold pools as are often associated with the cloud-arcs evident on days when these patterns are evident.

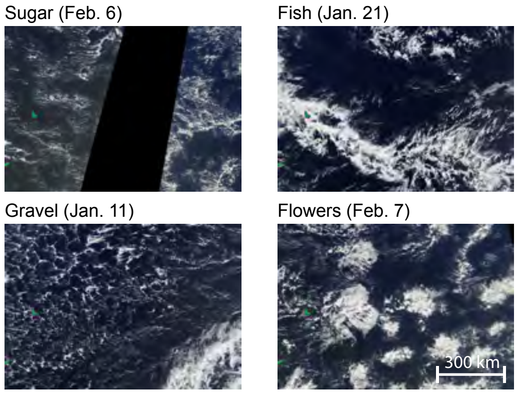

Figure 7. Meso-scale patterns of shallow convection in the trades as defined by Stevens, Bony, et al. (2020) and observed in Moderate Resolution Imaging Spectroradiometer images of true color channel composite. Green overlay indicates landmasses with Barbados in the western part of the image.

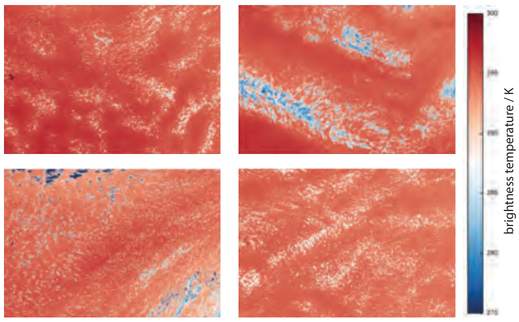

Figure 8. Overview of simulated satellite images of ICON-312m matching the cloud scenes shown in Fig. 7. Different to Fig. 7 the simulated infrared channel of ABI is shown.

Simulated *Flowers* are, however, not readily distinguishable from the *Sugar* scene in the simulations. The main deficiency appears to be the failure of the simulations to reproduce the stratiform layers observed in association with *Flowers*. This deficiency is not remedied by a factor of four refinement in the horizontal grid (see supplemental Fig. S1), as differences between the ICON-624m and the ICON-156m simulations are still substantially smaller than the finest resolution simulations and the observations. Past work Stevens et al. (2001), using more idealized configurations suggest that the development of stratiform layers is quite sensitive to the numerical representation of the very finest scales, rendering the ability of LES to differentiate in the development of stratiform layers, across patterns a critical test of the method.

3.2.2 Fractional coverage from neural networks

To objectively describe the capability of the simulations to represent the meso-scale cloud patterns, the synthetic satellite images are also classified by the neural network of Schulz et al. (2021). By comparing these classifications with those based on satellite observations, the short-comings of the simulation become more apparent.

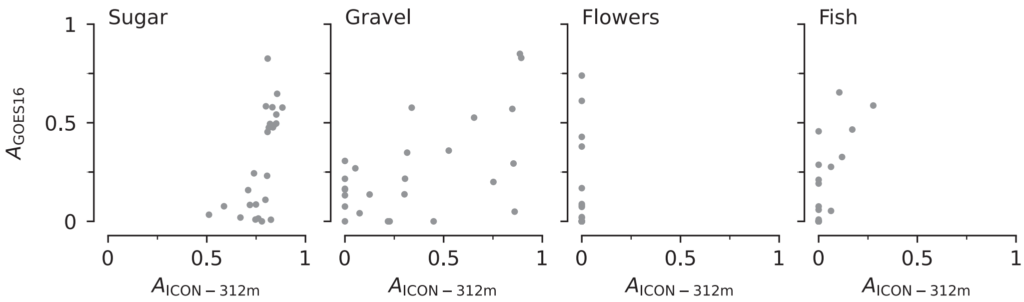

Figure 9. Daily mean area fraction covered by meso-scale patterns as identified by the neural network on actual (ABI) and simulated (ICON-312m) satellite images.

Fig. 9 shows the agreement in daily area fraction A of a particular pattern as identified in the simulation and the observations. Here we use the domain of ICON-156m (7.5N-17N and 60.25W-45W) as a common domain to get better statistics. A repetition of the analysis on the smaller domain did not reveal qualitative differences (not shown). The inference from the previous section that *Sugar* is too widespread can be confirmed by this analysis. Day to day variability in the area coverage of *Sugar* is much less in the simulations. It is present in nearly 80 percent of the domain on all days. In the observations, and in contrast, the area fraction ranges between 0% and 80%. This appears mostly compensated for by *Flowers*, which are not identified in the simulations, but are not infrequent, and on some days quite pronounced, in the observations. In case of *Fish*, the simulations also falls short in representing a comparable area fraction, albeit less markedly deficient than for the case of *Flowers*. Among all the patters, *Gravel* best matches the observations.

While most patterns do not show a strong dependence on resolution at the simulated scales, *Gravel* improves its match with the observed area-fraction, Fig. 10. The bias in the fractional coverage of *Gravel* relative to the observations reduces from 35%

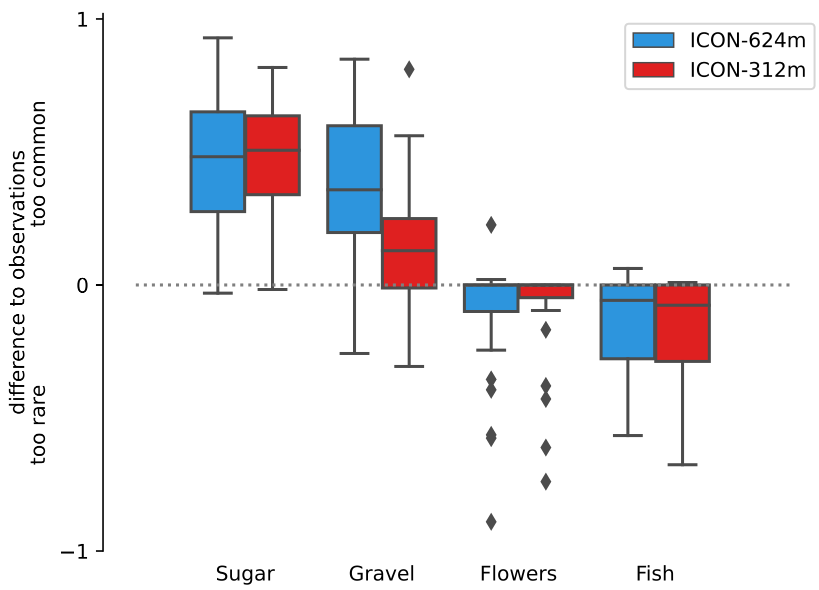

Figure 10. Difference in area-fraction occupied by patterns as identified by the neural network in the model simulations and observations. Boxes indicate the interquartile range around the median value. Whiskers extend this range by an additional 1.5 times the interquartile range. Outliers outside of the whiskers are marked with diamonds.

to 13%. In the coarser ICON-624m run some *Flowers* patches were identified, but remained largely unrepresented.

3.3 Cloudiness

3.3.1 Cloud cover

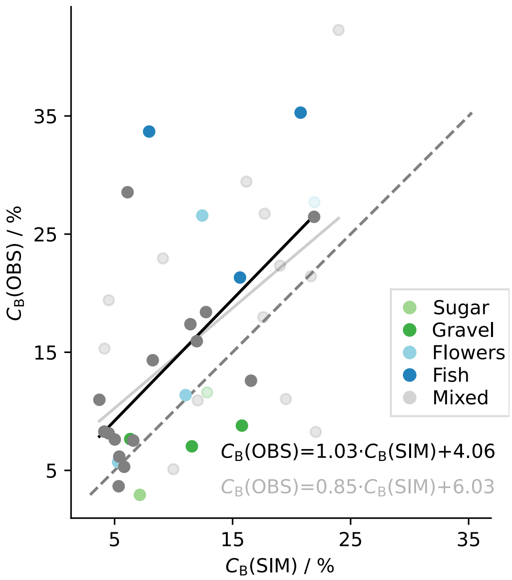

Figure 11. Daily cloud cover as derived from GOES-16 ABI and its simulated counterpart in ICON-312m. Colored markers indicate dominant meso-scale cloud patterns as detected in satellite observations. The identity line is dashed in grey. Linear fits are shown for all days (grey) and days without high clouds (black) and its intense markers.

A basic motivation for studying trade-wind clouds is to better understand what controls cloud amount, both in the mean and its variability. As discussed above, and in the other previously cited studies, cloud cover is one of the most distinguishing factors across the different meso-scale patterns. It is this aspect of the patterns that makes them interesting to study. In this section we explore how well the simulations represent the mean cloud cover, its vertical profile, its synoptic and diurnal variability, and how this varies with environmental changes accompanying the emergence of different patterns in the observations. Our focus in this section is on cloud cover. The effect of it and cloud physical properties on the radiative signature of clouds is discussed in § 3.6.

To compare the cloud cover of the simulations with satellite observations, we rely again on the brightness temperatures of measured and simulated satellite images. Similar to Bony et al. (2020) we define shallow clouds by a brightness temperature between 280 K and 290 K, and denote by C_B the fraction of the domain covered by such clouds.

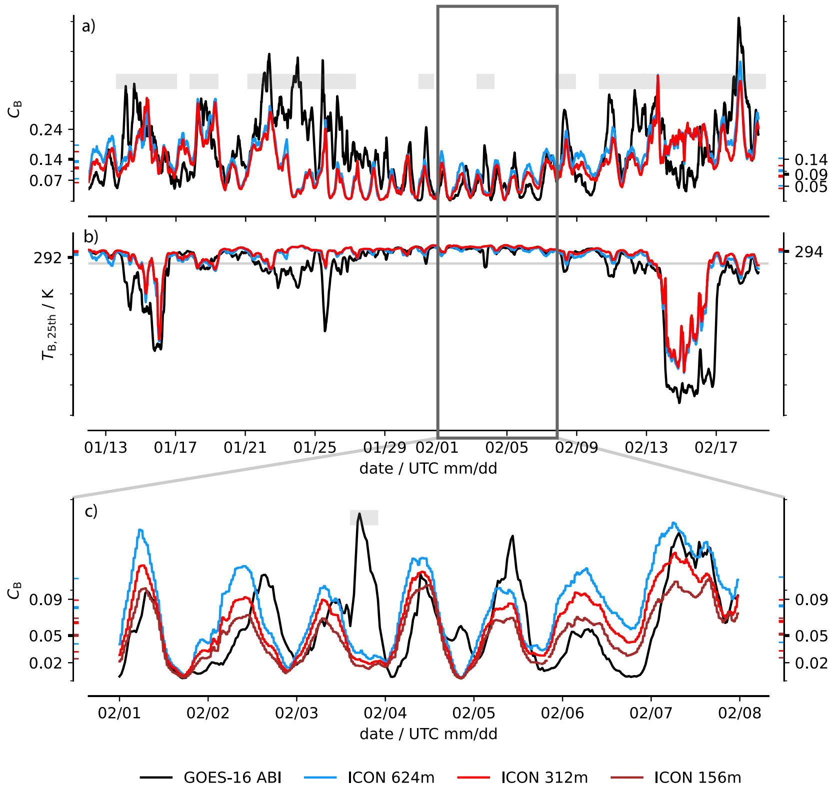

Figure 12. Timeseries of cloud cover (C_B) inferred from actual and synthetic satellite images (a) and the lower quantile of brightness temperature (T_B) within the domain as an indicator of high clouds (b). (c) magnifies the time period February 1 to February 7 and includes the result of ICON-156m. Periods that include high clouds based on the lower quantile of brightness temperature being below 290 K are indicated by gray bars in (a,c). The median and 25th/75th percentile are indicated by thick/thin labeled major ticks. The markers on the right y-axis exclude days with high clouds.

Day to day variability in C_B agrees well with GOES-16 ABI, Fig. 11, scatters simulated daily values of C_B against what was observed. The simulated cloud cover is biased slightly low compared to the observations, but changes in the simulated daily cloud-cover vary almost one-to-one (on average) with the observations.

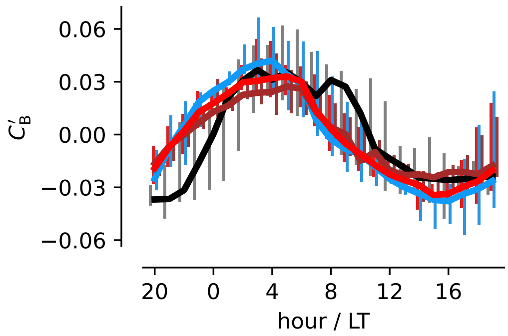

Figure 13. Median diurnal cycle as anomaly to the daily mean within the time-period shown in Fig. 12 without contributions from high-clouds.

Although the simulations appear to capture variations in day-to-day cloud cover on average, there is considerable variability, and there are days where the observed C_B are in the upper quantile of its distribution, while the simulated C_B is in its lower quantile. Discrepancies are most apparent in the time-series, e.g. between January 21 and January 27, in association with colder lower-quantile brightness temperatures (Fig. 12b) indicative that the domain is contaminated with high clouds. Cases where the lower-quantile drops below 290 K are marked with a gray horizontal bar in Fig. 12a. Fig. 12, however, also highlights that factor of two discrepancy in cloud amounts can appear on days without high-clouds, for instance on 6 Feb. 2020, which has been classified as dominated by *Sugar* in the observations.

The simulations appear to roughly capture both the variability of C_B across days, as it varies with synoptic conditions, and variability within a day. To better quantify the simulation of the diurnal cycle of C_B without the contributions of high clouds we focus on the 1-7 Feb period, as this is relatively free of high clouds and also allows an investigation of resolution sensitivity. The time-series of C_B over this period is presented in Fig. 12b, and as a composite in Fig. 13. The mean C_B over this period is observed to be 5.3% (GOES-16 ABI) and 8.3%, 6.5%, and 5.1% for ICON-624m, ICON-312m, and ICON-156m respectively. However, this improvement with resolution holds only true on average for this time-period. Across all days without high-clouds during the simulated period the observed cloud cover is 9.0 %, while the model simulates 10.2 % (ICON-624m) and 8.4 % (ICON-312m). Because the cloudiness reduces systematically with increasing resolution, the bias to the observations on a day-by-day basis varies and does not always improve. The coarser resolution run achieves particularly better agreement with the observations when stratiform clouds are observed. Previous work which shows a sensitivity to grid aspect ratio (Kazil et al., 2021, Stevens et al., 2001, 1999) emphasizes how for many of these quantities the resolution remains marginal or even insufficient to provide precise quantitative estimates.

The amplitude of the observed diurnal cycle is 7%, and 8%, 7% and 5% for ICON-624m, ICON-312m and ICON-156m, respectively. The simulations show a clearer maximum in cloudiness at about 04 LT, which decreases through the morning and into the early afternoon. In contrast, the observations show cloudiness to be more constant through the early morning hours, with some evidence of an early morning peak. This is attributable to strong peaks on particular days (Fig. 12) that are not represented by the simulations. Qualitatively our results agree with Vial et al. (2019) but show an overall lower amplitude in the diurnal cycle. Besides different definitions of cloudiness, the simulated time-period of the NARVAL campaign was particularly cloudy (Vial et al., 2019).

3.3.2 Vertical cloud distribution

The vertical distribution of cloudiness is important for structuring the cloud albedo, but also for the development of cloud microphysical processes. In addition to assessing how well this is represented across the EUREC^{4}A period we also explore how it varies as a function of the observed meso-scale pattern of cloudiness, as Schulz et al. (2021) documented systematic variations in the vertical structure of cloudiness across patterns.

For this purpose we examine the vertical distribution of cloudiness by means of the high-frequency (60 s) ICON-LEM column output (meteogram) at the location of the BCO. As described in Sec. 2.1.2, the output has been converted to reflectivity to facilitate comparison with the BCO radar data, for this reason we adopt echo fraction $C_{\mathrm{E}}(z)$ as our measure of cloudiness.

On average the simulated $C_{\mathrm{E}}(z)$, shows a typical trade-wind profile (Fig. 14a) with a peak in cloudiness at the lifting condensation level at around 800 m and a slowly decreasing cloudiness to the trade-inversion at about 2 km (Siebesma et al., 2003, Stevens et al., 2001). The simulations show a tendency toward a more bottom heavy profile of cloudiness, with an overestimate that is largest near the LCL and through the sub-cloud layer. This difference reduces with resolution, from 10 %(ICON-624m) to 5 %(ICON-312m).

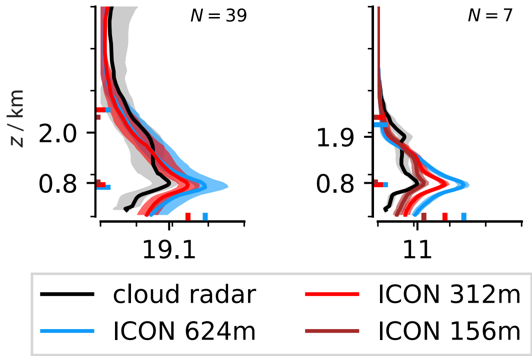

Figure 14. Cloud fraction variability for entire simulation period (a) and for the subsection of Feb 1 to Feb 7 when ICON-312m was also active (b). Standard error is shaded. Labeled ticks mark height and extent of maximum cloud fraction and height of the inversion based on the radar observations in former and soundings from Stephan et al. (2021) in the later. Colored ticks indicate the identical values for the simulations. The inversion height is defined as the height of the maximum vertical gradient of the liquid potential temperature (θ_l).

For the 1-7 Feb period, the differences are also apparent, but less so for the ICON-156m simulation (2 %) (Fig. 14b). These biases extend to the near surface echo fraction, which suggests that they are associated with precipitating hydrometeors, either drizzle or rain. The better correspondence to the observations with improved resolution is apparent at all levels, also in the near-surface echo fractions, and is consistent with earlier studies of more idealized cases (Stevens, Acquistapace, et al., 2020).

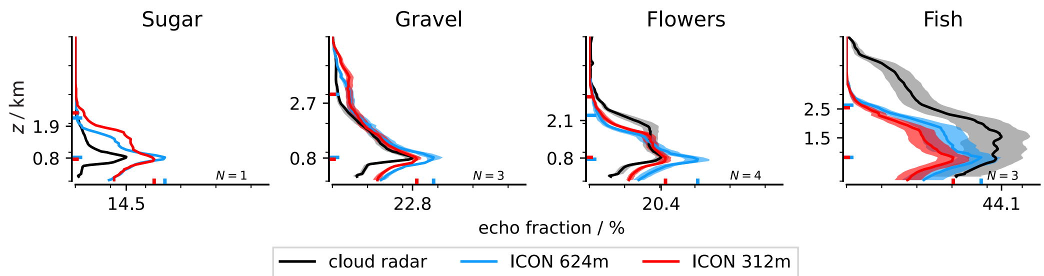

Figure 15. As Fig. 14 but here for days where meso-scale patterns were identified in the observations following Schulz (2022). N defines the number of days found for each group.

Compositing $C_{\mathrm{E}}(z)$ over days associated with observations of particular meso-scale pattern allows us to test the pattern dependent skill of the simulations. The separation reveals that the differences between simulations and observations do depend on the observed meso-scale context. The best resembled profile of $C_{\mathrm{E}}(z)$ is the one of *Gravel*. The cloudiness at the lifting condensation level is well matched, especially for the higher resolution run. Further aloft it follows closely the observed distribution. For *Gravel* the main discrepancies are below the lifting condensation level, where the echo fraction indicates more precipitation.

The simulations overestimate the near-surface echo fraction (which we associate with rain or drizzle) not only for *Gravel*, but also for *Sugar*, *Flowers* and the overall average as well. The underestimation of rain frequency in case *Fish*, along with its generally lower vertical extent, hint to a reduced activity of the remaining frontal system that is thought to structure the *Fish* patterns (Schulz et al., 2021). This analysis also points out how the simulations are limited by sample size for large-scale patterns such as *Fish*. Only one *Fish* passed the Barbados Cloud Observatory, albeit over three days between January 21 and January 23. Nonetheless, given the point-wise comparison, co-location biases make it difficult to establish the source of differences between the observed and simulated profiles. The supplemental movie shows that this *Fish* pattern was well developed and passed over the observatory also in the simulations (`https://www.doi.org/10.5281/zenodo.7567204`). However, it also reveals that in the simulations the pattern developed stronger in the east and decayed earlier in the west where the BCO is located. This development explains the shallower and more suppressed convection that resembles *Sugar* on January 24th and the reduced occurrence of deeper (3 km to 4 km) clouds in the mean.

The issue of representing the cloud fraction at the base of the trade-wind inversion, z_{i}, becomes again apparent and especially visible in the case of *Flowers*. $C_{\mathrm{E}}(z_{\mathrm{i}})$ is particularly underestimated. The simulations also struggle to represent *Sugar*. While this pattern distinguishes itself from *Gravel*, as in the observations through a lack of deeper clouds, the profile of $C_{\mathrm{E}}(z < 2\,\mathrm{km})$ is more similar in the simulated *Sugar* and *Gravel* than is observed, this includes values of $C_{\mathrm{E}}(z = 0\,\mathrm{m})$, which for the observed cases of *Sugar* vanish, but which remain similar between *Gravel* and *Sugar* in the observations.

3.4 Precipitation

While the above sections have shown that the echo fraction below cloud base and therefore the rain frequency is too high on average, their daily anomalies agree reasonably well. (Fig. 16). Both observed and simulated anomalies approach 30 %. The outliers seen in Fig. 16 in the lower right quadrant are for January 18 and January 19, when the clouds were organized by a large-scale system that developed a strong large-scale contrast in cloudiness with the Barbados Cloud Observatory residing mostly in the clear-sky area. In the simulation the organization was less strong and positioned closer to the location of the Barbados Cloud Observatory leading to the large offset. The opposite is true for January 23 during the passage of the *Fish* pattern, when the pattern passed the BCO closer in reality (upper left quadrant).

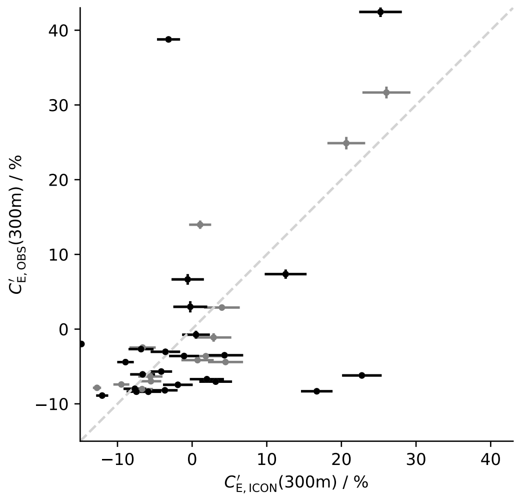

Figure 16. Echo fraction at 300 m ASL at the Barbados Cloud Observatory location is representative of the rain fraction. Daily anomalies of rain fraction to the entire time series are plotted for radar observations and the ICON-312m simulation. Standard error is calculated based on rolling windows of four hours and indicated as daily average. Grey dashed line indicates the one-to-one line. Grey markers represent days with high clouds.

The distribution of echo intensities contributing to the echo fraction differ more substantially between the observations and simulations. This is shown in Fig. 17 which compares the echo intensity distribution at three heights. Below cloud base the observed echo intensities are more uniformly distributed, with echos between −50 dBZ to −25 dBZ being found as often as echoes between −25 dBZ to 0 dBZ. In the simulations it is rather rare to sample echos less than −25 dBZ, which is compensated by echos around −15 dBZ being twice as frequent as observed. Also stronger echos, indicative of more intense rain, are much less likely in the simulations, although differences are exaggerated by the saturation of the near-surface radar return at about 15 dBZ. Near cloud base the observations also show the emergence of a second mode, with the frequency of echos increasing as the reflectivity decreases below −25 dBZ. The opposite behavior in the simulations likely highlights the inability of the simulations to represent the deliquescence of large cloud condensation nuclei, which were shown by Klingebiel et al. (2019) to be quite common at the BCO. At 1500 m where echos are expected to reflect the onset of more active coalescence of the lofted hydrometeors, rather than a mixture of precipitation from above with the in-situ microphysical development of aerosol and cloud droplets, the match between the simulations and observations is better, albeit perhaps less variable in the simulations. This comparison suggests that matching the observed echo distributions presents itself as a critical test of the ability of LES to represent the microphysical evolution of trade-wind clouds.

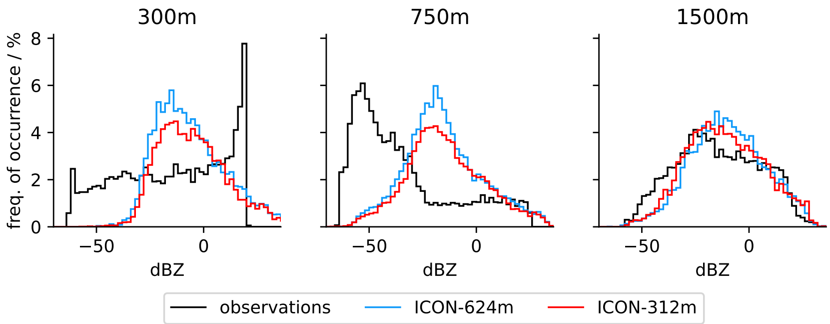

Figure 17. Reflectivity histograms based on radar observations at the BCO and their synthetic counter-part for the simulations within the subcloud-layer (300 m), around the cloud base height (750 m) and above (1500 m).

3.5 Environmental influence on cloud fraction

As demonstrated by Nuijens et al. (2009) for trade-wind clouds observed during the RICO field study (Rauber, Stevens, et al., 2007), and Schulz et al. (2021) for mesoscale patterns of cloudiness, cloud amount co-varies with differences in environmental factors such as wind-speed or stability. Cloud fractions tend to be less in anomalously warm environments with low wind-speeds, while higher echo-fractions are often present in colder regimes under strong inversions and with stronger winds. Here, we test the co-variability of cloudiness with the environmental factors, albeit independent of the classification of patterns of cloudiness.

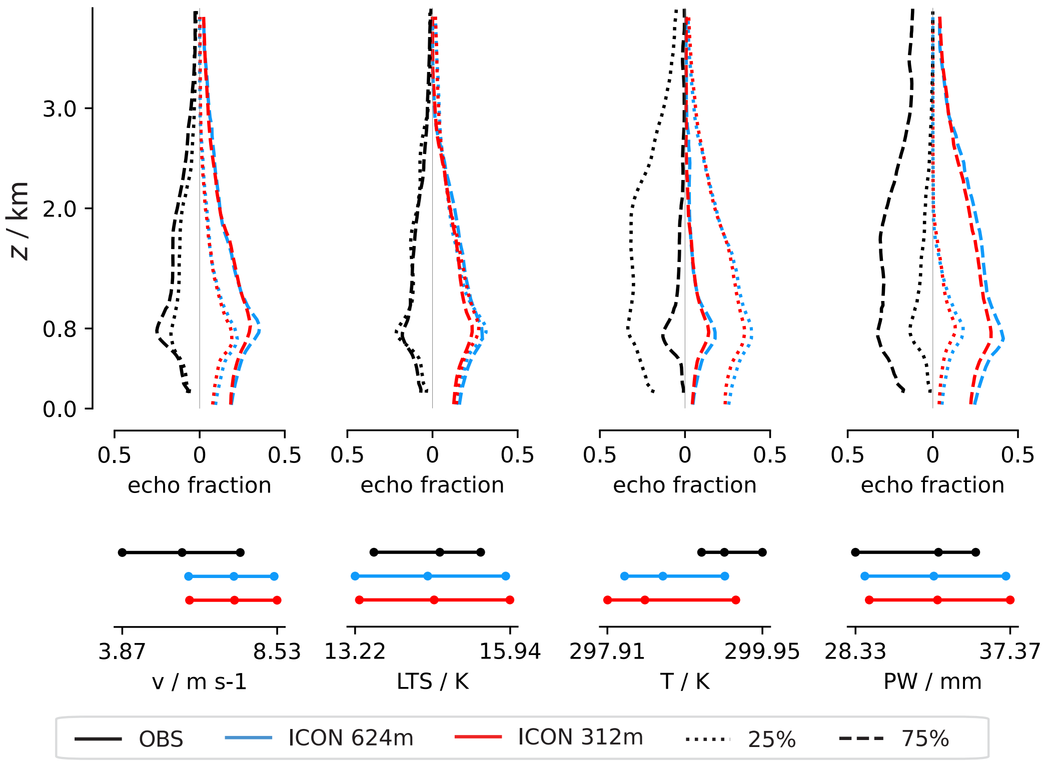

Figure 18. Dependence of echo fraction on daily averaged environmental conditions (left to right: 10m wind speed, 2m-temperature, lower tropospheric stability and precipitable water) in both observations (black profiles) and simulations (colored profiles). The 25th-75th percentile range of environmental conditions are shown in the lower panel. Observations: black; ICON-624m: red; ICON-312m: orange.

Fig. 18 illustrates how $C_{\mathrm{E}}(z)$ varies with the three most common environmental conditions correlating with meso-scale variability, wind-speed, temperature and inversion strength, as identified by Bony et al. (2020) for both observations and simulations. In addition, we also explore co-variability of $C_{\mathrm{E}}(z)$ precipitable water (PW), as Nuijens et al. (2009) identified this as a controlling factor. Despite differences in the distribution of environmental factors (Fig. 18b), the near mirror symmetry between the observed profile of the 25th and 75th percentiles of $C_{\mathrm{E}}(z)$ and those simulated, measures the similarity between the two, something which is relatively in dependent of resolution. Temperature and precipitable water separates the cloud-fraction profiles best compared to LTS and wind speed. The sensitivity to precipitable water was also seen (in their case for θ_e) in the analysis of trade-wind clouds during RICO (Nuijens et al., 2009). While the simulations lack cloudiness around 2km in the low temperature case, and to some extent at low wind-speeds, the shallower clouds in the warm case are well resembled. Notably, the precipitation change is captured well when comparing the echo fractions of the lowest levels, but is generally too strong.

Although wind-speed has been identified to distinguish well between the different meso-scale patterns (Bony et al., 2020, Schulz et al., 2021) it mostly acts along patterns of similar cloud fractions (see Fig. 3 of Bony et al. (2020)) and separates *Gravel* from *Sugar* and *Fish* from *Flowers*. The similar profiles for both wind-speed quantiles in the observations is consistent with such behavior. The simulations show more of a differentiation, something also seen in the analysis by Nuijens et al. (2009) across the lower and middle terciles in cloudiness. Based on the analysis of meso-scale patterns of variability we would expect a greater differentiation among quantiles for the LTS, this is however not evident in either the observations or simulations, similar to what was found by Nuijens et al. (2009) and perhaps indicative of a lack of *Flowers* in both that and the present study.

3.6 Radiative effects

In this section we return to the question of cloud cover, as seen through the effect of clouds on the irradiances at the top of the atmosphere. These are, after all, the effects that underpin our interests in trade-wind clouds in the first place, and the patterns of cloudiness which are shown to modulate them.

Here we use the Clouds and the Earth's Radiant Energy System (CERES) Synoptic (SYN) 1 degree (SYN1deg) product which is enhanced with geostationary satellite data to capture the diurnal cycle (NASA/LARC/SD/ASDC, 2017). This introduces a potential bias as the interpretation of the geostationary data is based on modelling, whose fidelity on a day-to-day basis has (to our knowledge) not been investigated but is of importance when capturing the cloudiness of meso-scale cloud pattern in the trades (Vial et al., 2021).

Overall the simulations reasonably represent the day-to-day variability in the top-of-atmosphere irradiances. Fig. 19(a) shows how well the simulated top-of-atmosphere outgoing irradiances matches observations. The distribution is well balanced along the identity line, more so when cases with high-clouds are excluded. There is a net bias of about $5.5\,\mathrm{W\,m^{-2}}$, with the simulations cooling less than observed. In both the observations and the simulations, *Flowers* with their large stratiform layers (at least in the observations) and dry free-troposphere are associated with days that radiate more heat to space in the net as compared to *Gravel* days which are close to a net zero at the top of the atmosphere.

Simulated cloud radiative effects agree less well with the observations. Fig. 19(b), and (c) compare the daily anomalies, the net cloud radiative effect is dominated by the shortwave component and is presented in panel (d). Day-to-day variability in the longwave cloud radiative effect is much smaller in the simulations than in the observations, and shows very little relationship to the observed. These biases may arise from thin high-clouds in the observations that are not present in the simulations, and whose effects are, by virtue of their thinness, not identified in our efforts to filter days with possible high-cloud contamination. Even for the shortwave, the correlation between the observed and simulated cloud radiative effects is in the right sense, but not strong, and substantially less than that for the cloud amount. While our suspicion is that most of the biases arise from deficiencies in the simulations, given the way in which CERES must infer the diurnal cycle using angular distribution models, which may not be optimized for shallow clouds, it is also not immediately obvious to what extent the measurements are free of random errors.

As to be expected the net cloud radiative effect, is dominated by the short-wave component, but due to the deleterious effect of the long-wave cloud radiative effects, its simulated value correlates even less well with the observations. This analysis, underlines the difficulty of quantitatively simulating cloudiness, even with relatively fine mesh and large domain simulations, perhaps not something that is unexpected given the sensitivity of idealized simulations to the details of their implementation (numerics) (Stevens et al., 2001) and assumptions that remain in parameterized processes.

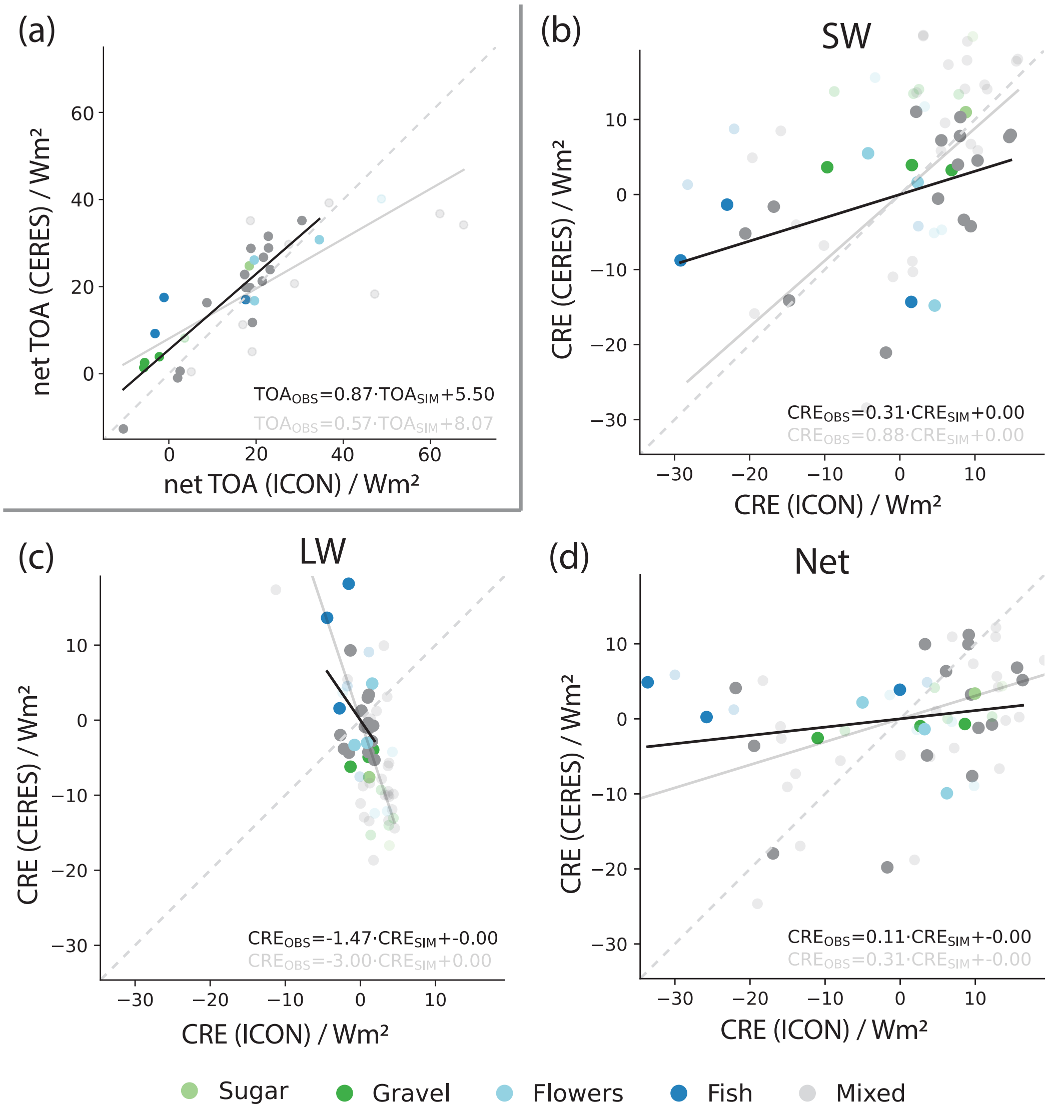

Figure 19. (a) Net TOA fluxes of ICON-312m and CERES. (b,c,d) Daily anomaly of cloud radiative effect relative to the studied time-series average (faint markers: entire time-series; bold markers: days with low clouds only). Colored markers indicate dominant meso-scale cloud patterns as detected in satellite observations.

4 Conclusion

The ability of large-eddy simulation to quantitatively capture the mean structure of the trade-wind boundary layer, and the clouds that form within it, has been evaluated using data collected from the EUREC^{4}A field study.

Simulations were performed using the ICON model for 41 days from 10 January through 20 February 2020, over exceptionally large domains spanning the trade-wind domain and time period of EUREC^{4}A. Simulations were performed using multiple nests, with gridspacings of 312 m and 624 m, and with a yet finer inner nest for an additional seven day period between 1 and 7 February. The domain of the inner most nest spanned slightly more than 1000 km in the zonal direction, from 59.75°W to 50°W, and 500 km, from 10.5°N to 15.5°N in the meridional direction. The coarser mesh simulations encompassed progressively larger domains and provided lateral boundary conditions for the finer mesh. The coarsest mesh simulation received boundary forcings from a yet larger domain storm-resolving simulation (1250 m horizontal mesh). For this purpose the last 24 h of the storm resolving simulations were used, with these initialized at 0 UTC for every day and run for 40 h, with lateral boundary conditions interpolated between hourly updates of the reanalysis. The simulations are, if not unprecedented, unusual by virtue of their computational intensity, and the way they are constrained to capture the large-scale meteorological conditions as observed during EUREC^{4}A.

The simulation strategy, whose large domains enable the simulations to capture the scale at which trade-wind clouds organize, combined with the measurement strategy that statistically sampled the boundary layer over a large meso-scale region, provides a basis for quantifying the ability of coarse grid large-eddy simulation to represent the trade-wind boundary layer and trade wind clouds, something that, until now, has not been possible. The evaluation is further aided through the use of the forward operators RTTOV and PAMTRA to allow for a more quantitative comparison to both satellites and surface-based cloud radars. The satellite simulator (RTTOV) also enabled the use of a neural-network based pattern classification scheme trained on labeled observations.

The simulations are shown to reasonably represent the mean structure, as measured by the profile of winds, clouds, and thermodynamic variables of the trade-wind boundary layer measured during EUREC^{4}A. The match is not perfect, with the simulated boundary layer being cooler (1 K) and drier (1 g kg^{-1}) than the observed boundary layer, for reasons that may partly be due to a 0.4 K to 0.6 K under-estimate of the sea-surface temperatures by the reanalysis. The simulated boundary layer also shows less differentiation between the cloud and inversion layer than is observed, also in the mean. The simulations are able to capture differences in the meso-scale structure underlying different meso-scale patterns of cloudiness, but have difficulty in fully representing the cloud-forms that accompany these patterns (Schulz et al., 2021). In particular there is a deficit of stratiform clouds in association with the *Flowers* pattern, following the taxonomy of Stevens, Bony, et al. (2020), and *Sugar* is more wide-spread than observed.

The observed coverage of low-clouds, of about 9.0%, is well captured by the simulations, ironically somewhat more so on the coarser grids, as cloud cover progressively decreases from 10.2% to 8.4% for the 624 m and 312 m simulations respectively, suggesting that the goodness of fit at coarser resolution may benefit from compensating errors. The simulations also well represent day-to-day variability in cloudiness, and the mean diurnal cycle – whose amplitude is about 6 %, or half of the mean – increasingly so as resolution is refined.

The vertical distribution of cloudiness, as measured by the echo fraction at the Barbados Cloud Observatory and compared to a vertically pointing cloud radar at that site, agrees reasonably well with the observations. The simulated cloud fractions maximize near cloud base, at about 800 m, and decay over a roughly 2 km cloud layer. The simulations tend to slightly over-estimate cloud base cloudiness and under-estimate cloudiness near the base of the trade inversion, with again too little differentiation between the cloud and inversion layers. The vertical structure of cloudiness improves markedly with the refinement of horizontal resolution, but even at 156 m grid-spacing the inversion layer and its clouds are still poorly differentiated from the cloud layer. Compositing across canonical patterns of mesoscale organization highlight the challenge the simulations have in representing *Sugar*. While prevalent in the simulations, simulated *Sugar* is characterized by cloud-base cloud fractions that are a factor of two to large, and simulated *Flowers* days show little sign of enhanced stratiform cloudiness. All in all, the simulations mainly differentiate *Sugar* from *Flowers* from *Gravel* by progressively deepening the cloud layer, but not otherwise changing the vertical distribution of echo fraction, in marked contrast to the observations. Despite the difficulty in differentiating among meso-scale cloud patterns, the simulations show cloudiness varying with environmental conditions in ways that mimic the data, with precipitable water, near surface temperatures and wind speeds most clearly influencing cloud amount.

The simulations tend to over-estimate the echo fractions in the sub-cloud layer, indicative of too much, perhaps too light, precipitation. They also represent a much narrower distribution of echo intensities at cloud base and in the sub-cloud layer than is seen in the radar data. The day-to-day variability, i.e., the variation in precipitation with synoptic conditions, appears to be reasonably well captured, as is the reflectivity distribution within the cloud layer. If anything, the simulations show a greater sensitivity to wind speed than is observed.

Despite the on average well simulated cloud cover and net TOA radiation, day-to-day anomalies in cloud radiative effects as measured by CERES prove difficult to reproduce. Day-to-day variability in long-wave cloud radiative effects is uncorrelated, or perhaps even negatively correlated with the observations, and short-wave cloud radiative effects are only weakly correlated with the data. The cause for the poor match between observed and simulated cloud radiative effects merits further investigation, also with possible limitations in the data in mind.

For investigating these effects, but also other biases such as the overly cool and dry boundary layer, and the difficulty in developing a stratiform cloud layer, we show that the seven day period between 1-7 February may suffice. This period is particularly useful for a more in depth study as it encompasses two periods of *Flowers* and one of *Sugar*, which presents some of the greatest challenges for the simulation. Past experience suggests that using less diffusive numerical methods can favor the development of stratiform clouds, but often also in situations like for *Sugar*, when they do not form. Hence, simulating both with quantitative fidelity poses a critical test for hecto-meter scale simulations and the turbulence and microphysical models that accompany them.

EUREC^{4}A measured a wealth of data, only a small amount of which is used here. For instance additional cloud radar data is available from research vessels and research aircraft, as is water vapor profiling, and passive microwave measurements capable of constraining cloud water. This analysis has only scratched the surface of the available data, but sufficiently so to reveal the main challenges for LES to quantitatively represent observed boundary layer clouds in the trades, and in particular their tendency to form patterns of meso-scale organization.

5 Open Research

The simulation output and observations from the EUREC^{4}A campaign are freely available and can be easily accessed via the EUREC^{4}A-Intake catalog at `https://github.com/eurec4a/eurec4a-intake` as described at `howto.eurec4a.eu`. The processing scripts are available at `doi.org/10.5281/zenodo.7591546`. GOES-16 Advanced Baseline Imager Level 1b radiances are available at `doi.org/10.7289/V5BV7DSR` and were converted with Raspaud et al. (2019) to brightness temperatures. MODIS imagery originates from the NASA Worldview application (`https://worldview.earthdata.nasa.gov`), part of the NASA Earth Observing System Data and Information System (EOSDIS). The ERA5 output used in this study (Hersbach, H. et al., 2018) has been provided by the Climate Data Store. The Clouds and the Earth's Radiant Energy System (CERES) product used is available at NASA/LARC/SD/ASDC (2017)

6 Acknowledgement

The authors are grateful to the members of the Tropical Cloud Observation group for maintaining the Barbados Cloud Observatory and continuously increasing its valuable data-set. The authors thank Daniel Klocke for conducting the ICON-SRM simulations and his valuable comments regarding ICON in general. Robert Vicari is thanked for implementing an updated version of the satellite forward operator interface into ICON. This work used resources of the Deutsches Klimarechenzentrum (DKRZ) and the authors are thankful for the granted compute time and storage.

References

Albright, A. L., Bony, S., Stevens, B., & Vogel, R. (2022, September). Observed Subcloud-Layer Moisture and Heat Budgets in the Trades. *Journal of the Atmospheric Sciences*, *79*(9), 2363–2385. doi: 10.1175/JAS-D-21-0337.1

Atlas, R. L., Bretherton, C. S., Blossey, P. N., Gettelman, A., Bardeen, C., Lin, P., & Ming, Y. (2020). How Well Do Large-Eddy Simulations and Global Climate Models Represent Observed Boundary Layer Structures and Low Clouds Over the Summertime Southern Ocean? *Journal of Advances in Modeling Earth Systems*, *12*(11), e2020MS002205. doi: 10.1029/2020MS002205

Baldauf, M., Seifert, A., Förstner, J., Majewski, D., Raschendorfer, M., & Reinhardt, T. (2011, December). Operational Convective-Scale Numerical Weather Prediction with the COSMO Model: Description and Sensitivities. *Monthly Weather Review*, *139*(12), 3887–3905. doi: 10.1175/MWR-D-10-05013.1

Bony, S., & Dufresne, J.-L. (2005). Marine boundary layer clouds at the heart of tropical cloud feedback uncertainties in climate models. *Geophysical Research Letters*, *32*(20), n/a–n/a. doi: 10.1029/2005GL023851

Bony, S., Schulz, H., Vial, J., & Stevens, B. (2020). Sugar, Gravel, Fish, and Flowers: Dependence of Mesoscale Patterns of Trade-Wind Clouds on Environmental Conditions. *Geophysical Research Letters*, *47*(7), e2019GL085988. doi: 10.1029/2019GL085988

Bony, S., & Stevens, B. (2019, March). Measuring Area-Averaged Vertical Motions with Dropsondes. *Journal of the Atmospheric Sciences*, *76*(3), 767–783. doi: 10.1175/JAS-D-18-0141.1

Bony, S., Stevens, B., Ament, F., Bigorre, S., Chazette, P., Crewell, S., ... Wirth, M. (2017, September). EUREC4A: A Field Campaign to Elucidate the Couplings Between Clouds, Convection and Circulation. *Surveys in Geophysics*, *38*(6), 1529–1568. doi: 10.1007/s10712-017-9428-0

Bretherton, C. S., & Blossey, P. N. (2017). Understanding Mesoscale Aggregation of Shallow Cumulus Convection Using Large-Eddy Simulation. *Journal of Advances in Modeling Earth Systems*, *9*(8), 2798–2821. doi: 10.1002/2017MS000981

Brient, F., Schneider, T., Tan, Z., Bony, S., Qu, X., & Hall, A. (2016, July). Shallowness of tropical low clouds as a predictor of climate models' response to warming. *Clim Dyn*, *47*(1-2), 433–449. doi: 10.1007/s00382-015-2846-0

Dipankar, A., Stevens, B., Heinze, R., Moseley, C., Zängl, G., Giorgetta, M., & Brdar, S. (2015). Large eddy simulation using the general circulation model ICON. *Journal of Advances in Modeling Earth Systems*, *7*(3), 963–986. doi: 10.1002/2015MS000431

Gassmann, A. (2013). A global hexagonal C-grid non-hydrostatic dynamical core (ICON-IAP) designed for energetic consistency. *Quarterly Journal of the Royal Meteorological Society*, *139*(670), 152–175. doi: 10.1002/qj.1960

George, G., Stevens, B., Bony, S., Pincus, R., Fairall, C., Schulz, H., ... Radtke, J. (2021, November). JOANNE: Joint dropsonde Observations of the Atmosphere in tropical North atlaNtic meso-scale Environments. *Earth System Science Data*, *13*(11), 5253–5272. doi: 10.5194/essd-13-5253-2021

George, G., Stevens, B., Bony, S., Vogel, R., & Naumann, A. K. (2022, September). *Ubiquity of shallow mesoscale circulations in the trades and their influence on moisture variance.* Earth and Space Science Open Archive. doi: 10.1002/essoar.10512427.1

Hartmann, D. L., Ockert-Bell, M. E., & Michelsen, M. L. (1992, November). The Effect of Cloud Type on Earth's Energy Balance: Global Analysis. *Journal of Climate*, *5*(11), 1281–1304. doi: 10.1175/1520-0442(1992)005⟨1281:TEOCTO⟩2.0.CO;2

Heinze, R., Dipankar, A., Henken, C. C., Moseley, C., Sourdeval, O., Trömel, S., ... Quaas, J. (2017). Large-eddy simulations over Germany using ICON: A comprehensive evaluation. *Quarterly Journal of the Royal Meteorological Society*, *143*(702), 69–100. doi: 10.1002/qj.2947

Hersbach, H., Bell, B., Berrisford, P., Biavati, G., Horányi, A., Muñoz Sabater, J., ... Thépaut, J-N. (2018). *ERA5 hourly data on single levels from 1979 to present.* Copernicus Climate Change Service (C3S) Climate Data Store (CDS). doi: 10.24381/cds.adbb2d47

Heus, T., & Seifert, A. (2013, August). Automated tracking of shallow cumulus clouds in large domain, long duration large eddy simulations. *Geosci. Model Dev.*, *6*(4), 1261–1273. doi: 10.5194/gmd-6-1261-2013

Jacob, M., Kollias, P., Ament, F., Schemann, V., & Crewell, S. (2020, November). Multilayer cloud conditions in trade wind shallow cumulus – confronting two ICON model derivatives with airborne observations. *Geoscientific Model*

Development, *13*(11), 5757–5777. doi: 10.5194/gmd-13-5757-2020

Kazil, J., Christensen, M. W., Abel, S. J., Yamaguchi, T., & Feingold, G. (2021). Realism of Lagrangian Large Eddy Simulations Driven by Renalysis Meteorology: Tracking a Pocket of Open Cells Under a Biomass Burning Aerosol Layer. *Journal of Advances in Modeling Earth Systems*, *13*(12), e2021MS002664. doi: 10.1029/2021MS002664

Klingebiel, M., Ghate, V. P., Naumann, A. K., Ditas, F., Pöhlker, M. L., Pöhlker, C., ... Stevens, B. (2019, February). Remote Sensing of Sea Salt Aerosol below Trade Wind Clouds. *Journal of the Atmospheric Sciences*, *76*(5), 1189–1202. doi: 10.1175/JAS-D-18-0139.1

Mech, M., Maahn, M., Kneifel, S., Ori, D., Orlandi, E., Kollias, P., ... Crewell, S. (2020, September). PAMTRA 1.0: The Passive and Active Microwave radiative TRAnsfer tool for simulating radiometer and radar measurements of the cloudy atmosphere. *Geoscientific Model Development*, *13*(9), 4229–4251. doi: 10.5194/gmd-13-4229-2020

Mlawer, E. J., Taubman, S. J., Brown, P. D., Iacono, M. J., & Clough, S. A. (1997, July). Radiative transfer for inhomogeneous atmospheres: RRTM, a validated correlated-k model for the longwave. *Journal of Geophysical Research: Atmospheres*, *102*(D14), 16663–16682. doi: 10.1029/97JD00237

NASA/LARC/SD/ASDC. (2017, September). *CERES and GEO-Enhanced TOA, within-atmosphere and surface fluxes, clouds and aerosols 1-Hourly terra-aqua Edition4A.* NASA Langley Atmospheric Science Data Center DAAC.

Nuijens, L., Medeiros, B., Sandu, I., & Ahlgrimm, M. (2015, June). The behavior of trade-wind cloudiness in observations and models: The major cloud components and their variability. *Journal of Advances in Modeling Earth Systems*, *7*(2), 600–616. doi: 10.1002/2014MS000390

Nuijens, L., Serikov, I., Hirsch, L., Lonitz, K., & Stevens, B. (2014, October). The distribution and variability of low-level cloud in the North Atlantic trades. *Quarterly Journal of the Royal Meteorological Society*, *140*(684), 2364–2374. doi: 10.1002/qj.2307

Nuijens, L., Stevens, B., & Siebesma, A. P. (2009, July). The Environment of Precipitating Shallow Cumulus Convection. *Journal of the Atmospheric Sciences*, *66*(7), 1962–1979. doi: 10.1175/2008JAS2841.1

Rasp, S., Schulz, H., Bony, S., & Stevens, B. (2020, November). Combining Crowdsourcing and Deep Learning to Explore the Mesoscale Organization of Shallow Convection. *Bulletin of the American Meteorological Society*, *101* (11), E1980-E1995. doi: 10.1175/BAMS-D-19-0324.1

Raspaud, M., Hoese, D., Lahtinen, P., Dybbroe, A., Finkensieper, S., Roberts, W., ... Valentino, A. (2019, June). *Pytroll/satpy: Version 0.16.0.* Zenodo. doi: 10.5281/zenodo.3250583

Rauber, R. M., Ochs, H. T., Di Girolamo, L., Göke, S., Snodgrass, E., Stevens, B., ... Twohy, C. H. (2007, December). Rain in Shallow Cumulus Over the Ocean: The RICO Campaign. *Bulletin of the American Meteorological Society*, *88* (12), 1912–1928. doi: 10.1175/BAMS-88-12-1912

Rauber, R. M., Stevens, B., Ochs, H. T., Knight, C., Albrecht, B. A., Blyth, A. M., ... Zuidema, P. (2007, December). Rain in Shallow Cumulus Over the Ocean: The RICO Campaign. *Bulletin of the American Meteorological Society*, *88* (12), 1912–1928. doi: 10.1175/BAMS-88-12-1912

Riehl, H. (1954). *Tropical meteorology.* McGraw-Hill.

Saunders, R., Hocking, J., Turner, E., Rayer, P., Rundle, D., Brunel, P., ... Lupu, C. (2018, July). An update on the RTTOV fast radiative transfer model (currently at version 12). *Geoscientific Model Development*, *11* (7), 2717–2737. doi: 10.5194/gmd-11-2717-2018

Schulz, H. (2022, March). C^{3}ONTEXT: A Common Consensus on Convective OrgaNizaTion during the EUREC^{4}A eXperimenT. *Earth System Science Data*, *14* (3), 1233–1256. doi: 10.5194/essd-14-1233-2022

Schulz, H., Eastman, R., & Stevens, B. (2021). Characterization and Evolution of Organized Shallow Convection in the Downstream North Atlantic Trades. *Journal of Geophysical Research: Atmospheres*, *126* (17), e2021JD034575. doi: 10.1029/2021JD034575

Seifert, A., & Beheng, K. D. (2006, February). A two-moment cloud microphysics parameterization for mixed-phase clouds. Part 1: Model description. *Meteorology and Atmospheric Physics*, *92* (1), 45–66. doi: 10.1007/s00703-005-0112-4

Siebesma, A. P., Bretherton, C. S., Brown, A., Chlond, A., Cuxart, J., Duynkerke, P. G., ... Stevens, D. E. (2003, May). A Large Eddy Simulation Intercomparison Study of Shallow Cumulus Convection. *Journal of Atmospheric Sciences*, *60* (10), 1201–1219. doi: 10.1175/1520-0469(2003)60⟨1201:ALESIS⟩2.0.CO;2

Stephan, C. C., Schnitt, S., Schulz, H., Bellenger, H., de Szoeke, S. P., Acquistapace, C., … Stevens, B. (2021, February). Ship- and island-based atmospheric soundings from the 2020 EUREC^{4}A field campaign. *Earth System Science Data*, *13*(2), 491–514. doi: 10.5194/essd-13-491-2021

Stevens, B., Ackerman, A. S., Albrecht, B. A., Brown, A. R., Chlond, A., Cuxart, J., … Stevens, D. E. (2001, July). Simulations of Trade Wind Cumuli under a Strong Inversion. *Journal of the Atmospheric Sciences*, *58*(14), 1870–1891. doi: 10.1175/1520-0469(2001)058⟨1870:SOTWCU⟩2.0.CO;2

Stevens, B., Acquistapace, C., Hansen, A., Heinze, R., Klinger, C., Klocke, D., … Zängl, G. (2020). The Added Value of Large-eddy and Storm-resolving Models for Simulating Clouds and Precipitation. *Journal of the Meteorological Society of Japan. Ser. II*, *98*(2), 395–435. doi: 10.2151/jmsj.2020-021

Stevens, B., Bony, S., Brogniez, H., Hentgen, L., Hohenegger, C., Kiemle, C., … Zuidema, P. (2020). Sugar, gravel, fish and flowers: Mesoscale cloud patterns in the trade winds. *Quarterly Journal of the Royal Meteorological Society*, *146*(726), 141–152. doi: 10.1002/qj.3662

Stevens, B., Bony, S., Farrell, D., Ament, F., Blyth, A., Fairall, C., … Zöger, M. (2021, August). EUREC^{4}A. *Earth System Science Data*, *13*(8), 4067–4119. doi: 10.5194/essd-13-4067-2021

Stevens, B., Farrell, D., Hirsch, L., Jansen, F., Nuijens, L., Serikov, I., … Prospero, J. M. (2016, May). The Barbados Cloud Observatory: Anchoring Investigations of Clouds and Circulation on the Edge of the ITCZ. *Bulletin of the American Meteorological Society*, *97*(5), 787–801. doi: 10.1175/BAMS-D-14-00247.1

Stevens, B., Giorgetta, M., Esch, M., Mauritsen, T., Crueger, T., Rast, S., … Roeckner, E. (2013). Atmospheric component of the MPI-M Earth System Model: ECHAM6. *Journal of Advances in Modeling Earth Systems*, *5*(2), 146–172. doi: 10.1002/jame.20015

Stevens, B., Lenschow, D. H., Faloona, I., Moeng, C.-H., Lilly, D. K., Blomquist, B., … Thornton, D. (2003, October). On entrainment rates in nocturnal marine stratocumulus. *Q.J.R. Meteorol. Soc.*, *129*(595), 3469–3493. doi: 10.1256/qj.02.202

Stevens, B., Moeng, C.-H., Ackerman, A. S., Bretherton, C. S., Chlond, A., de Roode, S., … Zhu, P. (2005, June). Evaluation of Large-Eddy Simulations via

Observations of Nocturnal Marine Stratocumulus. *Monthly Weather Review*, *133*(6), 1443–1462. doi: 10.1175/MWR2930.1

Stevens, B., Moeng, C.-H., & Sullivan, P. P. (1999, December). Large-Eddy Simulations of Radiatively Driven Convection: Sensitivities to the Representation of Small Scales. *Journal of the Atmospheric Sciences*, *56*(23), 3963–3984. doi: 10.1175/1520-0469(1999)056⟨3963:LESORD⟩2.0.CO;2

vanZanten, M. C., Stevens, B., Nuijens, L., Siebesma, A. P., Ackerman, A. S., Burnet, F., ... Wyszogrodzki, A. (2011). Controls on precipitation and cloudiness in simulations of trade-wind cumulus as observed during RICO. *Journal of Advances in Modeling Earth Systems*, *3*(2). doi: 10.1029/2011MS000056

Vial, J., Vogel, R., Bony, S., Stevens, B., Winker, D. M., Cai, X., ... Brogniez, H. (2019, October). A New Look at the Daily Cycle of Trade Wind Cumuli. *Journal of Advances in Modeling Earth Systems*, *11*(10), 3148–3166. doi: 10.1029/2019MS001746

Vial, J., Vogel, R., & Schulz, H. (2021). On the daily cycle of mesoscale cloud organization in the winter trades. *Quarterly Journal of the Royal Meteorological Society*, *147*(738), 2850–2873. doi: 10.1002/qj.4103

Vogel, R., Albright, A. L., Vial, J., George, G., Stevens, B., & Bony, S. (2022, December). Strong cloud–circulation coupling explains weak trade cumulus feedback. *Nature*, *612*(7941), 696–700. doi: 10.1038/s41586-022-05364-y

Wan, H., Giorgetta, M. A., Zängl, G., Restelli, M., Majewski, D., Bonaventura, L., ... Förstner, J. (2013, June). The ICON-1.2 hydrostatic atmospheric dynamical core on triangular grids – Part 1: Formulation and performance of the baseline version. *Geoscientific Model Development*, *6*(3), 735–763. doi: 10.5194/gmd-6-735-2013

Wick, G. A., Jackson, D. L., & Castro, S. L. (2023, January). Assessing the ability of satellite sea surface temperature analyses to resolve spatial variability – The northwest tropical Atlantic ATOMIC region. *Remote Sensing of Environment*, *284*, 113377. doi: 10.1016/j.rse.2022.113377

Zängl, G., Reinert, D., Rípodas, P., & Baldauf, M. (2015). The ICON (ICOsahedral Non-hydrostatic) modelling framework of DWD and MPI-M: Description of the non-hydrostatic dynamical core. *Quarterly Journal of the Royal Meteorological Society*, *141*(687), 563–579. doi: 10.1002/qj.2378

Supporting Information for "On the representation of shallow convection in the trades by large-domain, hecto-meter, large-eddy simulations"

Hauke Schulz[1,2], Bjorn Stevens[1]

[1]Max Planck Institute for Meteorology, Hamburg, Germany

[2]University of Washington/CICOES, Seattle, WA, USA

Contents of this file

Introduction This supporting information provides additional information about the ICON-624m simulation.

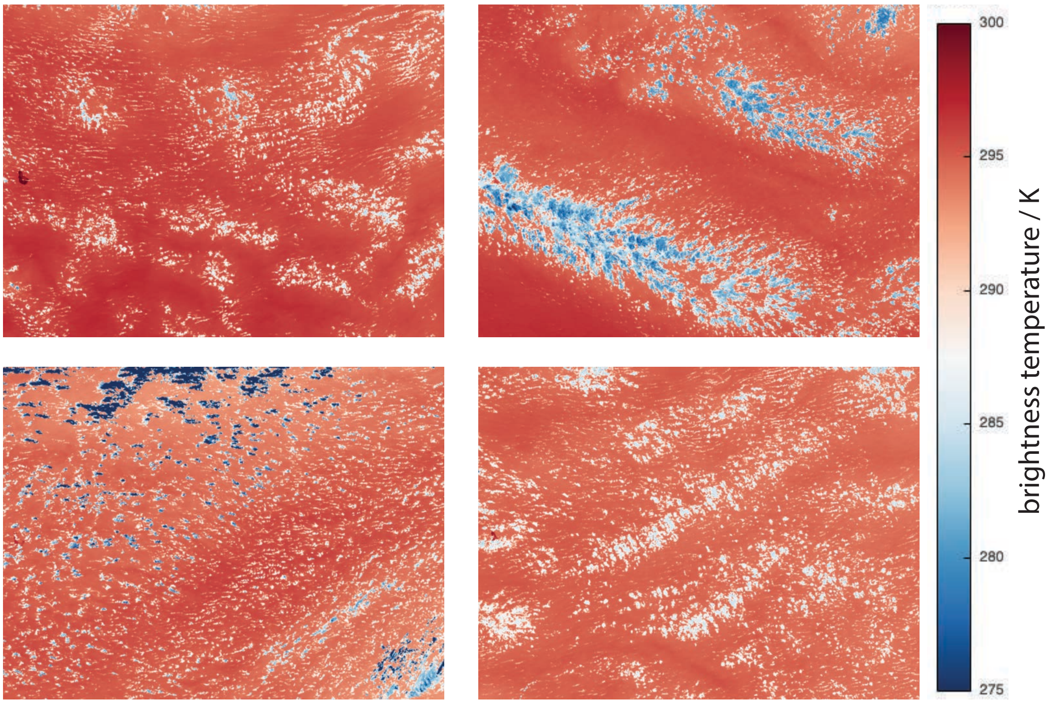

Figure S1. Like Fig. 8 but for the ICON-624m simulation.